Biochimica et Biophysica Acta 1797 (2010) 1327–1341

Contents lists available at ScienceDirect

Biochimica et Biophysica Acta

journal homepage: www.elsevier.com/locate/bbabio

4Pi microscopy reveals an impaired three-dimensional mitochondrial network of pancreatic islet β-cells, an experimental model of type-2 diabetes

Andrea Dlasková [a], Tomáš Špaček [a], Jitka Šantorová [a], Lydie Plecitá-Hlavatá [a], Zuzana Berková [b], František Saudek [b], Mark Lessard [c], Joerg Bewersdorf [d], Petr Ježek [a,*]

[a] Department of Membrane Transport Biophysics, No. 75, Institute of Physiology, Academy of Sciences of the Czech Republic, Prague, Czech Republic
[b] Institute of Clinical and Experimental Medicine, Prague, Czech Republic
[c] Imaging Science Services, The Jackson Laboratory, Bar Harbor, ME, USA
[d] Department of Cell Biology, Yale University, New Haven, CT, USA

ARTICLE INFO

Article history:
Received 27 October 2009
Received in revised form 26 January 2010
Accepted 1 February 2010
Available online 6 February 2010

Keywords:
3D morphology of mitochondrial network
4Pi microscopy
3D image analysis
Pancreatic β-cell
Type-2 diabetes
Morphological diagnostic

ABSTRACT

Insulin production in pancreatic β-cells is critically linked to mitochondrial oxidative phosphorylation. Increased ATP production triggered by blood glucose represents the β-cells' glucose sensor. Type-2 diabetes mellitus results from insulin resistance in peripheral tissues and impaired insulin secretion. Pathology of diabetic β-cells might be reflected by the altered morphology of mitochondrial network. Its characterization is however hampered by the complexity and density of the three-dimensional (3D) mitochondrial tubular networks in these cell types. Conventional confocal microscopy does not provide sufficient axial resolution to reveal the required details; electron tomography reconstruction of these dense networks is still difficult and time consuming. However, mitochondrial network morphology in fixed cells can also be studied by 4Pi microscopy, a laser scanning microscopy technique which provides an ~7-fold improved axial resolution (~100 nm) over conventional confocal microscopy. Here we present a quantitative study of these networks in insulinoma INS-1E cells and primary β-cells in Langerhans islets. The former were a stably-transfected cell line while the latter were transfected with lentivirus, both expressing mitochondrial matrix targeted redox-sensitive GFP. The mitochondrial networks and their partial disintegration and fragmentation are revealed by carefully created *iso*-surface plots and their quantitative analysis. We demonstrate that β-cells within the Langerhans islets from diabetic Goto Kakizaki rats exhibited a more disintegrated mitochondrial network compared to those from control Wistar rats and model insulinoma INS-1E cells. Standardization of these patterns may lead to development of morphological diagnostics for Langerhans islets, for the assessment of β-cell condition, before their transplantations.

1. Introduction

During the last two decades a handful of super-resolution microscopy techniques, that break the diffraction limit described by Abbe, have been developed. The first and best explored of these techniques, 4Pi microscopy, is enhancing the resolution of regular laser scanning confocal microscopy by utilizing two opposing high-numerical aperture objectives [1–9]. Combining them coherently for fluorescence excitation as well as detection (4Pi microscopy of 'type C') enables three-dimensional (3D) imaging of fixed biological samples with ~7-fold improved resolution (100 nm) in the *z*-axis direction [4]. Its lateral (xy) resolution equals to that of a conventional confocal microscope, given by the Abbe's condition $\Delta r = \lambda / 2NA$, with NA denoting the numerical aperture of the lens and λ the wavelength of light. For widely used green fluorescent protein (GFP) and high NA objectives this xy resolution is about 250 nm. Other techniques featuring even better resolution such as stimulated emission depletion (STED) microscopy [10–14] and single molecule localization-based techniques have been introduced to 2D [15–17] and more recently also 3D imaging [18–21] of biological structures including mitochondria [13,14]. All are discussed in detail in the Discussion section.

Our understanding of mitochondrial network morphology has made large progress in parallel with the development of confocal microscopy and its 3D imaging capabilities over the last two decades. Although certain indications were also provided by electron microscopy, the definitive proof that mitochondria of eukaryotic cells form a

Abbreviations: EM, electron microscopy; mRoGFP, mitochondrial matrix targeted redox-sensitive type 1 GFP; STED, stimulated emission depletion; T2DM, type-2 diabetes mellitus

* Corresponding author. Dept. No. 75, Membrane Transport Biophysics, Institute of Physiology, Academy of Sciences of the Czech Republic, Vídeňská 1083, 14220 Prague 4, Czech Republic. Tel.: +420 296442760; fax: +420 296442488.
E-mail address: jezek@biomed.cas.cz (P. Ježek).

0005-2728/$ – see front matter © 2010 Elsevier B.V. All rights reserved.
doi:10.1016/j.bbabio.2010.02.003

reticular network in most cell types was established based on the use of confocal microscopy (e.g. [22]). With living cells it has been recognized that the network is continuously remodeled by cycles of fission and fusion events, giving rise to various mitochondrial reticulum shapes [23–25]. The first super-resolution 3D imaging of mitochondrial networks has been reported by Egner et al. in yeast (*S. cerevisiae*) using 4Pi microscopy for imaging of their networks [9]. Utilizing 4Pi microscopy as well, details of a portion of mitochondrial reticulum recognizing tubule diameter of 200–400 nm in fixed mammalian cells have been reported by one of us [6]. Recently, we could show that mitochondria form a nearly completely interconnected tubular network with a fairly uniform tubule diameter of 270 ± 30 nm in insulinoma INS-1E cells and 280 ± 40 nm in hepatocellular carcinoma HEP-G2 cells, using a similar instrument [23]. In conclusion, it has been recognized that the 4Pi microscope's ~100 nm axial and ~250 nm lateral resolutions are sufficient to investigate the mitochondrial network morphology.

Why are studies of mitochondrial network morphology and cristae ultrastructure so important? Mitochondrial dysfunctions are indicated in numerous diseases originating from the oxidative stress, such as type-2 diabetes, cancer, atherosclerosis, heart ischemia, neurodegenerative diseases, including Alzheimer, Parkinson's disease, and multiple sclerosis, numerous mitopathies originating from defects of mitochondrial genome or mitochondria-related nuclear genome, and last, but not least, aging [24,25]. Moreover, a possible surprising existence of extra-mitochondrial membranes within the structure of myelin [26] and retina [27] has recently been opened. The inner-mitochondrial membrane-like structures, that were found in these classic-assumed neural tissues, have been proven to contain respiratory chain complexes as well as ATP synthase and it has been demonstrated that those structures are responsible for extra-mitochondrial respiration. If proven true, these extra-mitochondrial membranes might be examples of the extraordinary biogenesis of mitochondria. Not only these examples are waiting for utilization of super-resolution microscopy, which should undoubtedly provide a high impact on the progress in this field.

In addition, the role of mitochondria-derived oxidative stress and mitochondrial dysfunction has clearly been established in both type-1 and type-2 diabetes mellitus (T2DM) [28–35]. T2DM represents a world-wide epidemic. In its development T2DM is characterized by the insulin resistance in peripheral tissues, while concomitantly impaired insulin secretion is indicated in pancreatic β-cells. Recently, Finocchietto et al. [36] have shown that in skeletal muscle, upon insulin receptor signaling and concomitant glucose cell intake, mitochondrial respiration is transiently inhibited by nitric oxide synthesized by parallel activation of mitochondrial nitric oxide synthase. This leads to transient predominant use of glycolysis over oxidative phosphorylation, as it is rather sustained in cancer cells, cells adapted to hypoxia, and in fetal (stem) cells. Speculations lead to a possible cause of T2DM originating from an impaired plasticity of these transient oxidative phosphorylation inhibitions, being escalated into chronic protruded inhibitions and resulting in elevation of oxidative or nitrosative stress that lead to the pathway dysfunction.

Goto Kakizaki rats represent the suitable T2DM model, characterized by an onset of Langerhans islet pathology, indicated by islet hypertrophy with a decreasing number of insulin-secreting β-cells [37,38]. Possible causes of T2DM etiology in Goto Kakizaki rats might include mitochondrial dysfunction, besides the reduced expression of several exocytotic soluble N-ethylmalemide-sensitive factor attachment protein receptor (SNARE) complexes, such as Syntaxin-1A, SNAP-25, VAMP-2, and nSec1/munc18 proteins [38]. These complexes are important for the docking and fusion between insulin granules and β-cell membrane. Thus, a reduced number of docking granules would contribute to the impaired β-cell insulin secretion [38]. Also the decreased mtDNA content in Langerhans islets [39] and skeletal muscle [40] has been reported during development of Goto Kakizaki rats. It is not clear, whether it reflects diminished number of β-cells in an islet or number of mtDNA copies within a single remaining β-cell.

Mitochondrial dysfunction may be reflected by morphology of the mitochondrial network [24,25,41,42]. This rule may be applied also for pancreatic β-cells [43] in various diabetic states. Therefore, we attempted to evaluate possible hypothetical changes in β-cell mitochondrial network morphology in T2DM model of Goto Kakizaki rats. For this purpose, we have applied 4Pi microscopy in combination with lentiviral expression of redox-sensitive GFP targeted to the mitochondrial matrix space for 3D imaging of primary β-cells within the Langerhans islets. The comparison between samples isolated from control Wistar rats and diabetic Goto Kakizaki rats yielded a characteristic pattern of mitochondrial networks, namely their higher disintegration, reflecting the pathogenic changes in diabetic rats.

2. Materials and methods

2.1. Fusion protein constructs

The vector for mitochondrial addressing peptide (MAP)-conjugated redox-sensitive GFP (mRoGFP, a modified EGFP vector of "type 1" — see [44]) was a kind gift of Dr. Rossignol, Univ. Bordeaux 2, France. Note, the redox sensing property of mRoGFP was not employed here in the fixed cells. The mRoGFP sequence was inserted into the Viral Power system vector, the pLenti 6.3/V5-DEST vector (Invitrogen), while ligated by T4 DNA ligase (USB). Lentiviral particles were isolated as described below.

2.2. Lentiviral particle production

The pLenti 6.3/V5-DEST-based constructs have been multiplied, purified and used for lentiviral particle production according to the manufacturer's (Invitrogen) instructions. Thus the lentiviral stock (containing the packaged pLenti expression construct) was produced by co-transfecting the optimized packaging plasmid mix (packaging plasmids pLP1, pLP2, and pLP/VSVG, which supplies the helper functions as well as structural and replication proteins required to produce the lentiviruses) and our expression constructs into the 293LTV cell line, a derivative of the 293F Cell Line. The 293 LTV cell line is stably and constitutively expressing the SV40 large T antigen facilitating an optimal lentivirus production. Lipofectamine 2000 (Invitrogen) was used as the transfection reagent. The lentiviral stock was filtered and concentrated by PEG-it Virus Precipitation Solution (SBI) or using its separation by ultracentrifugation. Before proceeding to transduction and expression experiments, the titer of the lentiviral stock was determined, using fluorescence-activated cell sorting (Becton Dickinson LSR II).

2.3. Cell cultivation

Rat insulinoma INS-1E cells were a kind gift of Prof. Maechler, University of Geneva [45]. The INSE-1E cell line stably expressing mRoGFP was prepared using the Blasticidine-selection after the corresponding transfections. Transfected INS-1E cells were cultivated in RPMI 1640 medium with L-glutamine, without glucose supplemented with 10 mM HEPES, 1 mM pyruvate, 5% (v/v) fetal calf serum, 50 μM mercaptoethanol, 50 IU/ml penicillin, 50 μg/ml streptomycin, and 11 mM glucose.

2.4. Langerhans islet isolation

Wistar rats and Goto Kakizaki rats (Taconic, USA) were bred, housed, and sacrificed in accordance with the European Guidelines on Laboratory Animal Care and according to the Institute of Clinical and Experimental Medicine licensing committee approval. Goto Kakizaki rats were derived by embryo transfer from Danish (Aarhus) colony

established in 1994 from the original Tohoku University (Japan) colony initiated in 1975. 36 week old Goto Kakizaki rats were taken for this work. 4Pi microscopic images shown in this paper were done with islet samples isolated always from two Goto Kakizaki rats, weighing over 400 g and exhibiting hyperglycemia and crimpled intravenous glucose tolerance test (~20 mM glucose remained 60 min after glucose intake). Wistar rats were non-diabetic (normoglycemic and normal intravenous glucose tolerance test). Langerhans islet isolation was performed according to a standard protocol [46]. Pancreases were distended by an infusion of 15 ml collagenase (1 mg/ml; Sevapharma, Czech Republic) and the islets were separated from exocrine tissue by centrifugation in a Ficoll discontinuous gradient (Sigma). Purified islets were cultivated in RPMI 1640 medium without glucose supplemented with 10% fetal calf serum, 1% penicillin/streptomycin/L-glutamine, 1% HEPES, and 5 mM glucose, in a humidified CO_2 incubator at 37 °C and 5% CO_2 atmosphere. Islet viability was checked by propidium iodide and acridine orange methods.

2.5. Identification of β-cells within the Langerhans islets

Immunohistochemical staining against β-cell specific GLUT2 as a surface antigen has been performed to distinguish β-cells in the hypertrophic islets of Goto Kakizaki rats. Fixed islets were three times washed with phosphate buffer saline (PBS) and blocked with 5% donkey serum, 0.1 M glycine, 0.05% Tween 20 in PBS. Samples were incubated with rabbit anti-GLUT2 antibodies (1:200) in the blocking solution at 4 °C overnight. After 3-times washing in PBS containing 0.1 M glycine and 0.05% Tween 20, secondary Alexa 555-conjugated donkey anti-rabbit IgG antibodies were incubated with samples for two hours at room temperature. Final washing was done three times by PBS.

2.6. Preparation of samples for 4Pi microscopy

Transfected INS-1Ecells (cultured to 70% cell confluency) and non-transfected islets were cultured for 2–4 days on 4Pi quartz coverslips coated with poly-L-lysine. Islets had to be anchored onto the support, by letting the contaminating fibroblasts to attach to poly-L-lysine. Lentiviral particles were added only to the well attached islets and transfections were checked after ~24 h. The samples were then fixed with 0.025% glutaraldehyde and 4% paraformaldehyde for 60 min at 25 °C. The unreacted aldehydes were reduced by 1 mg/ml sodium borohydride (pH 8) three times for 15 min. Finally, the coverslips were washed three times in PBS. The coverslips with fixed and immunostained islets (cells) were mounted in the 4Pi sample holders

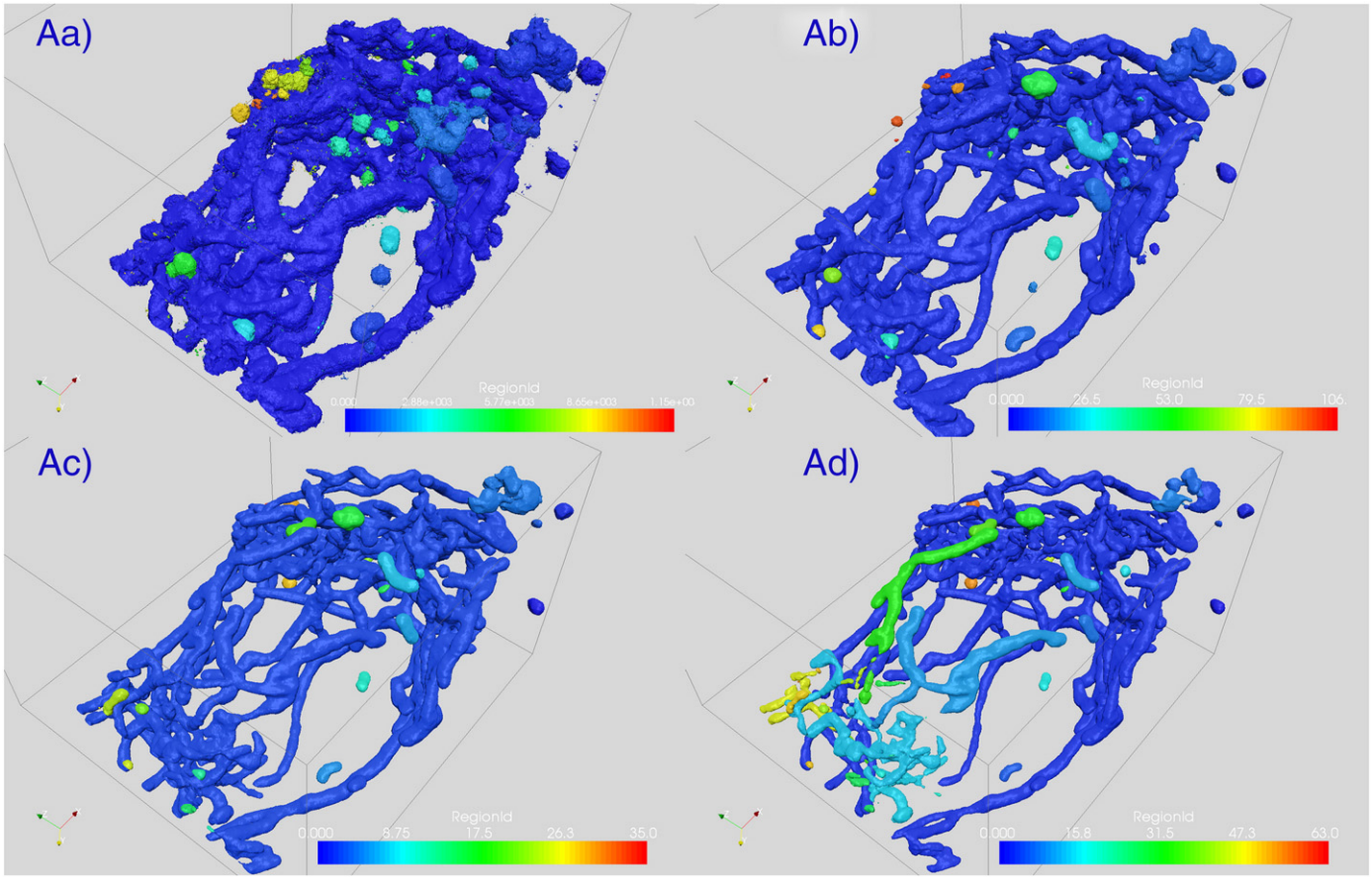

Fig. 1. Optimization of *iso*-surface thresholds I_T. A) Mitochondrial network in a half-body of INS-1E cell; B) mitochondrial network disintegrated by 20 μM rotenone in the whole INS-1E cell; C) intensity histograms. Color-coding illustrates the increasing number of objects with increasing *iso*-surface thresholds, I_T. The 4Pi microscopy data were projected into the 3D images using Paraview software, while varying I_T values among series of images — for A: I_T values of 5, 20, 45, and 65 are displayed in subpanels Aa), Ab), Ac), and Ad), respectively; note the inclusion of the noise at $I_T = 5$ and artificial fragmentation at $I_T = 65$. For B: I_T values of 5, 25, 50, 80, 120, and 160 have been taken as displayed in subpanels Bb), Bd), Be), Bf), Bg), and Bh), respectively. Panels Ba) and Bc) show the "radiosity" function displaying of the 3D data with I_T values of 5 and 25, respectively. Note, although even while imaging by conventional confocal microscopy gives for samples treated with 20 μM rotenone a complete disintegration picture [23], here at I_T values of 5 the displayed reconstruction shows a single interconnected reticulum. It is because at I_T values of 5 to 10 still a substantial noise signal is included in the 3D data. In turn, beginning $I_T = 25$, the displayed network is fragmented, thus corresponding to the most realistic images until at high $I_T > 100$ only backbone regions of tubules are displayed and further artificial disintegration is apparent. The $I_T = 160$ gives the image displaying only the highest intensity mRoGFP-field, probably the central matrix stalk not involving cristae. C) Intensity histograms: the three-point deconvolved 4Pi microscopy data are summarized in histograms of voxel counts of each intensity channel for INS-1E cell samples shown in panel A (Ca)), panel B (Cb)) and control β-cell sample displayed in Fig. 2a,b (Cc)), and diabetic β-cell sample displayed in Fig. 4e,f (Cd)).

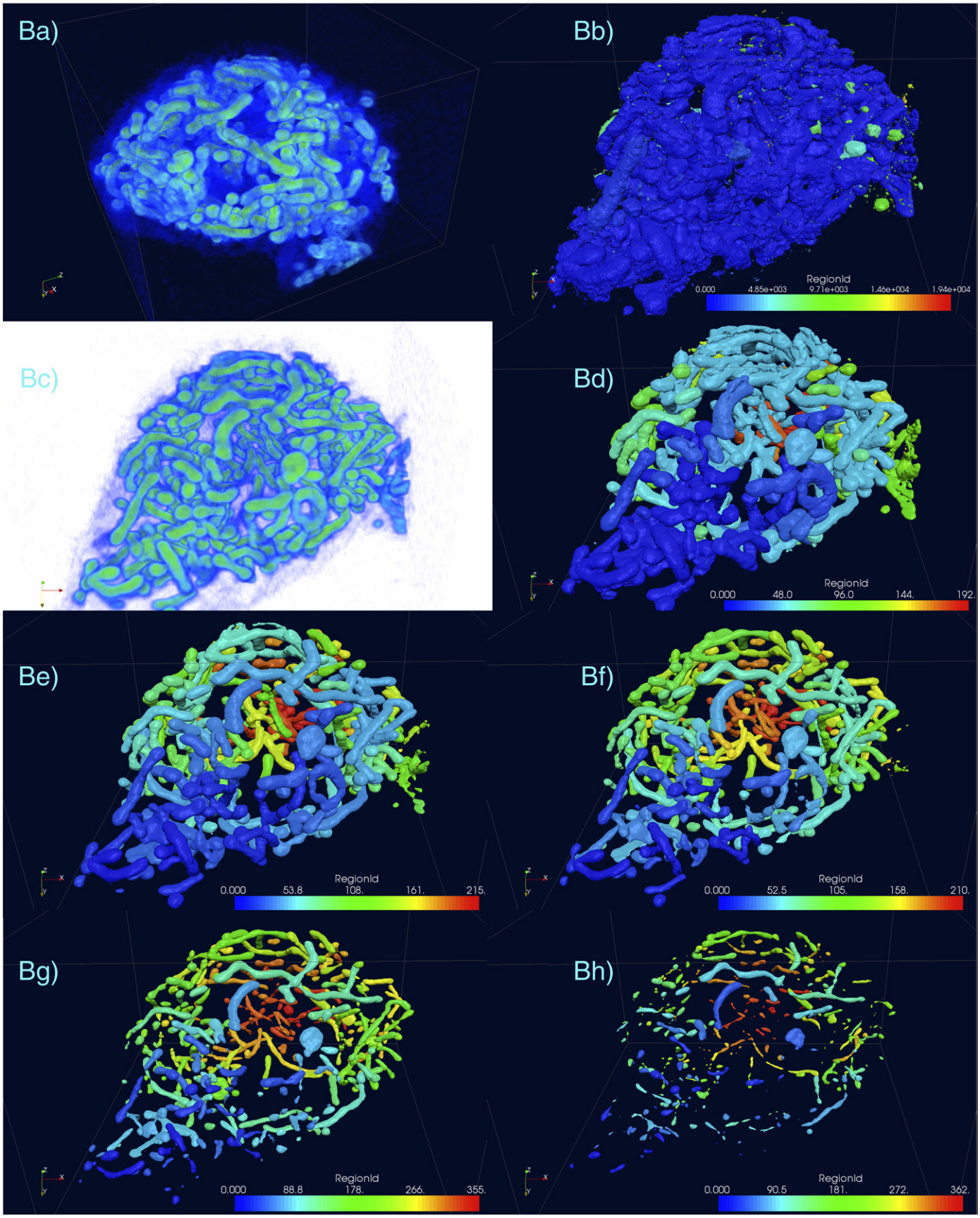

Fig. 1 (*continued*).

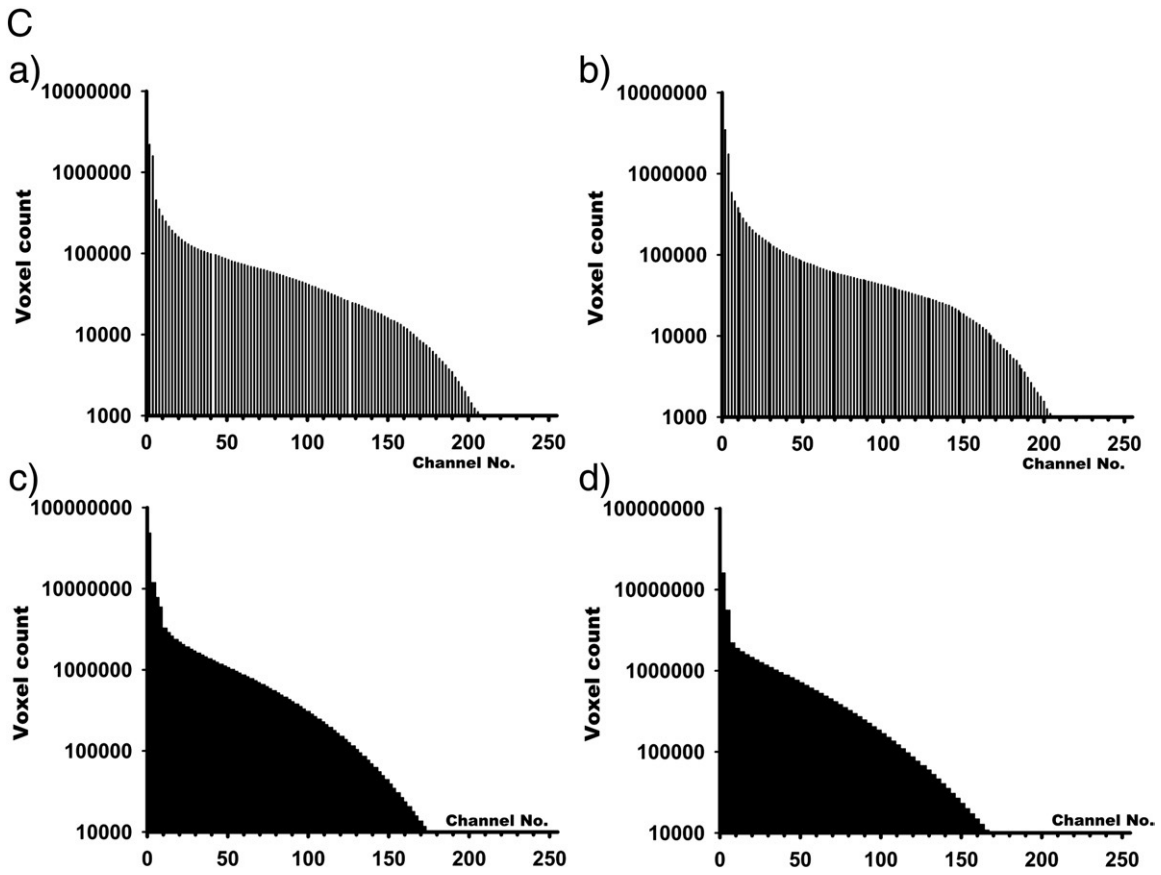

Fig. 1 (*continued*).

using 87.5% glycerol/PBS mounting medium with a refractive index of 1.460. Previous studies of mitochondria imaged with 4Pi microscopy have shown no morphological changes induced by this embedding [6]. The coverslip was then sealed to the sample holder using a two-component silicone glue (Twinsil, Picodent, Germany). A conventional confocal microscope (Leica TSC SP2, equipped with a PL APO 100×/1.4–0.7 oil immersion objective) was employed for quality control during sample preparation.

2.7. 4Pi microscopy

Data were collected with a Leica TCS 4PI microscope set up to operate in Type C mode, equipped with a pair of 100×/1.35 NA glycerol immersion objectives [4,23]. mRoGFP fluorescence was recorded using two-photon excitation at 906 nm wavelength (Chameleon laser, Coherent Laser Group) and photon counting avalanche photodiodes. A short pass SP700 filter followed by 525/50 (Chroma Technology Corp.) band pass filter was used in the detection path. The pinhole was set to 1 "Airy unit" while the beam expander was set to 3. The objective correction collars, focus alignment, and the interference phase of the microscope were adjusted for each individual sample. The embedding medium, in this case 87.5% glycerol/PBS with a refractive index of 1.460, was also used as the immersion medium to ensure continuity in the refractive index from objective to objective. Stacks of xz-images were recorded with a *y*-distance between neighboring slices of 31 nm. The pixel size in each xz image was chosen between 31 nm × 31 nm for control β-cells and 45 nm × 45 nm for diabetic β-cells. Stack dimensions were adapted to the cell size and were 15–24 μm × 10–14 μm × 12 μm for control β-cells and 24 μm × 24 μm × 12–17 μm for diabetic β-cells. In data post-processing, each stack was smoothed and 3-point deconvolved with the LCS software (Leica Microsystems).

2.8. 3D image analysis

3D image analysis has been done as described before [23] while 3D projections were created with Amira 5.2.2 software (Visage Imaging, Germany). Several 3D projection methods were used. First, Voltex plots were inspected, illustrating the representation of the 3D data ensemble after 3-point deconvolution. The most frequently used 3D projections in an *iso*-surface mode had to be optimized in order to avoid inclusion of noise on one hand and not cutting too much signal on the other hand when setting these thresholds. As clearly illustrated in Fig. 1A,B, the intensity threshold (I_T) should be adjusted to rather low values, but high enough to avoid a "rough" surface appearance of mitochondrial tubules with small blebs originating from included background. We want to point out that the resulting objects are not representing the ~100 nm resolution of the microscope anymore but are optimized for visualization of the tubular network and its connectivity. Varying I_T from 10 to e.g. 90 shows a characteristic artificial disintegration of the mitochondrial tubules. Setting the I_T to 90 means that only intensities of 90 and above (maximum 255) are taken into the account. Background noise automatically vanishes, but dim signal is also excluded. Analysis of proper I_T values, such as demonstrated in Fig. 1, is thus very important for judging the connectivity of mitochondrial network (see Results). Additionally, another 3D display has been utilized, using the "Autoskeleton" module of Amira 5.2.2. software package. This method provides another representation of disconnected parts of the network and transfers signal intensities into diameters of representative cylinders (Fig. 6). Alternatively, color-coding of separate objects was employed to count the numbers of each object types in 3D projections made using Paraview (Sandia Corporation, Kitware Inc., NM, USA), while varying I_T values. Volume of the network was taken as the number of voxels above I_T. By multiplying this number with the volume of a

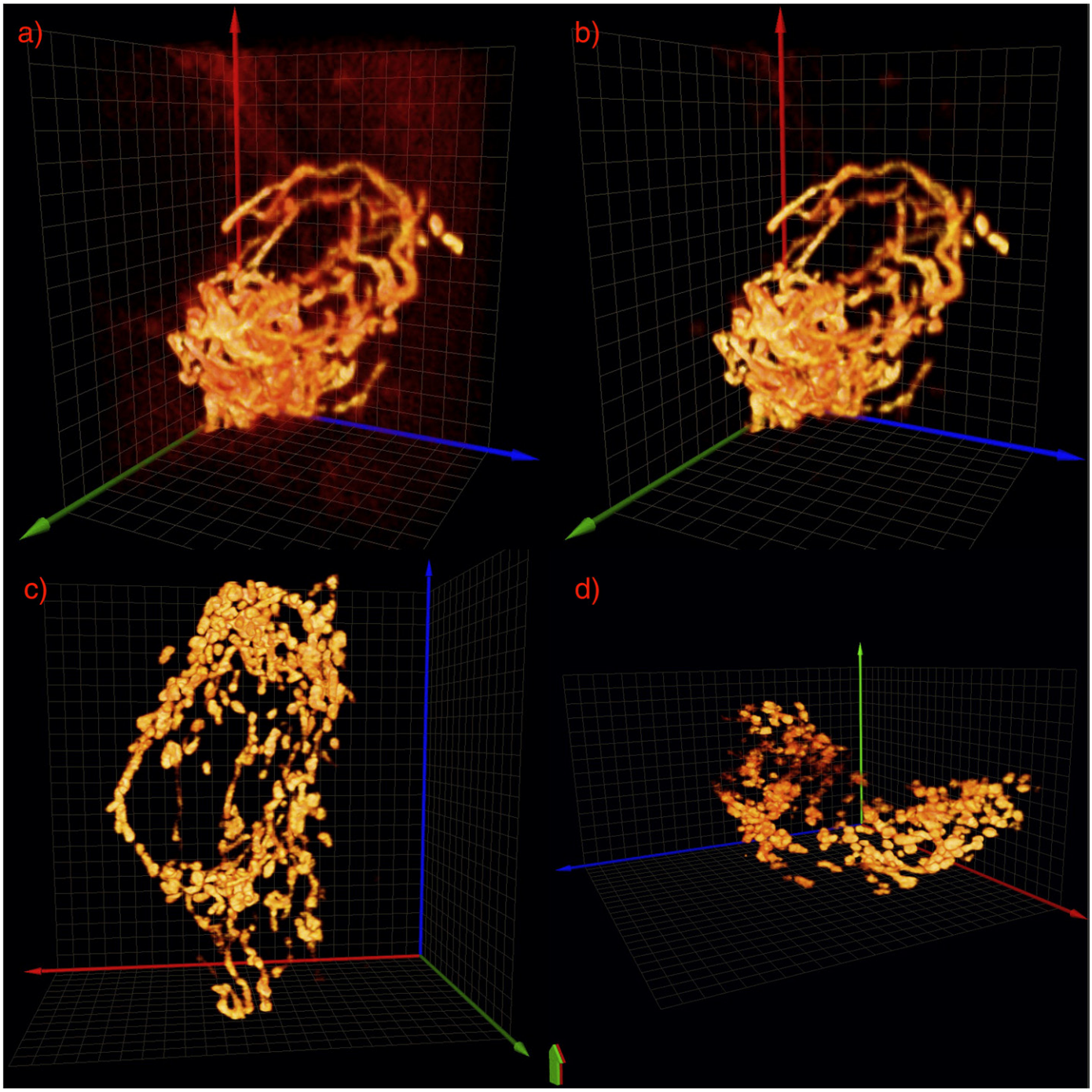

Fig. 2. 4Pi imaging of mitochondrial network of mRoGFP-transfected β-cells of Langerhans islets isolated from control Wistar rats (a,b) and diabetic Goto Kakizaki rats (c,d) — Voltex 3D projections. The three-point deconvolved data are shown for a single selected control β-cell of Langerhans islets isolated from non-diabetic Wistar rats (a) $I_T = 1$, b) $I_T = 15$; and for two examples of diabetic β-cells of Langerhans islets isolated from Goto Kakizaki rats (c,d), $I_T = 15$. Voltex 3D projections were created with Amira 5.2.2. A 1 μm 3D grid is shown in the background. Color-coding for axes: green — *Z* axis; red — *X* axis; blue — *Y* axis.

single voxel, an estimate for the volume of the tubular system can be generated. The "Autoskeleton" module has been used to sort the individual fragments and calculate their volumes. The diameters of tubules and other objects were either calculated by an "interferometric" method, *i.e.* from the point spread function of a triple image, containing side lobes [9], of randomly selected xz stacks; or by a "ruler" method, while measuring distances on the xz stacks.

Fig. 3. Conventional confocal 3D imaging and 2D imaging of living samples for mitochondrial network in mRoGFP-transfected non-diabetic and diabetic β-cells of Langerhans islets. Data were displayed in *iso*-surface plots (created with Amira 5.2.2) for 3D imaging (a–f) of living β-cells from lentivirally transfected Langerhans islets (with mRoGFP), isolated from control (Wistar) rats (a–d) and from diabetic Goto Kakizaki rats (e,f). A 1 μm 3D grid is shown in the background. Color-coding for axes is different than in Fig. 2: green — *Y* axis; red — *X* axis; blue — *Z* axis. Panels g) and h): 2D imaging of control (g) and diabetic β-cells (h). Conventional confocal microscopy was performed on a Leica TSC SP2 instrument, equipped with a PL APO 100×/1.4–0.7 oil immersion objective and single-photon excitation (488 nm).

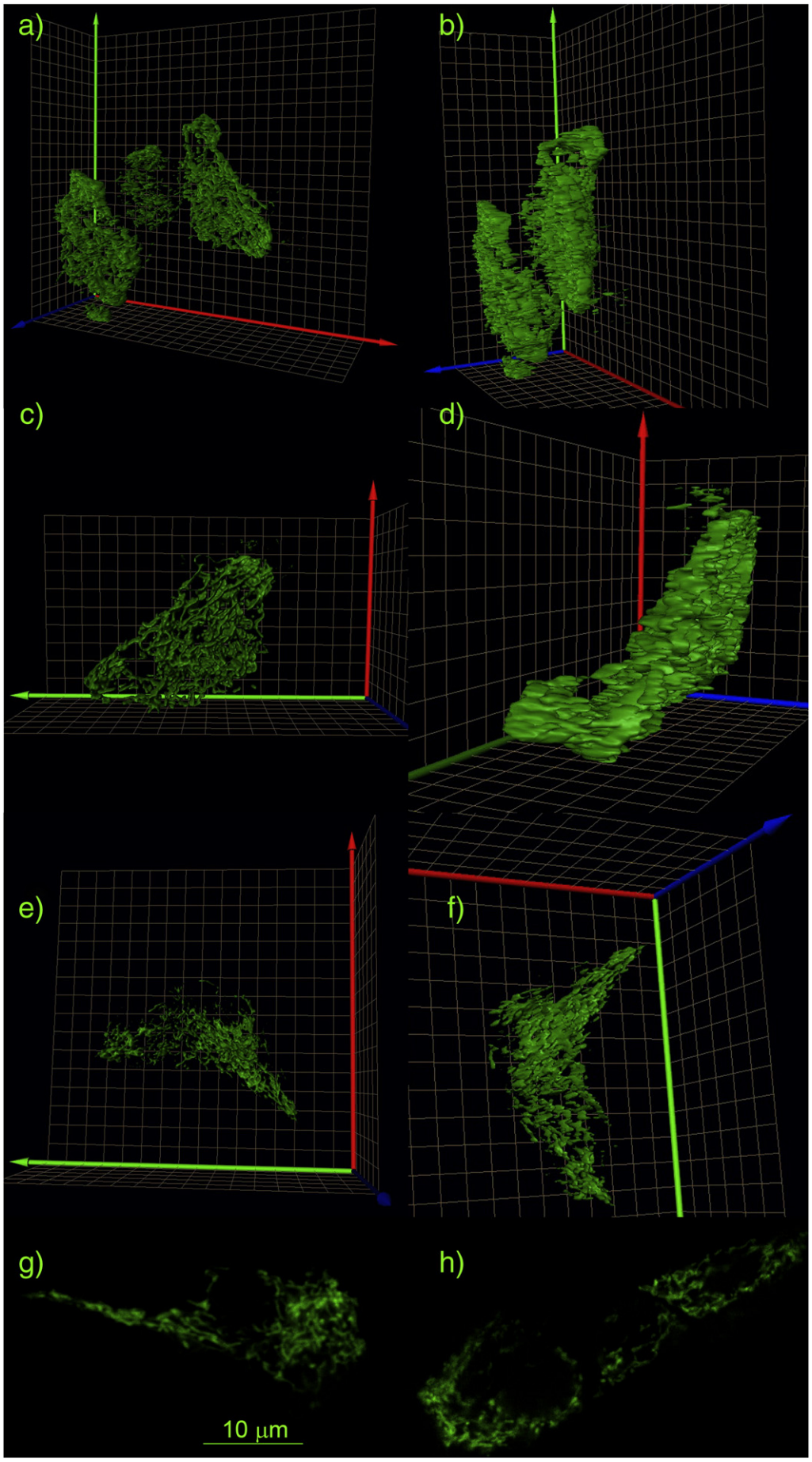
a)
b)
c)
d)
e)
f)
g)
h)
10 μm

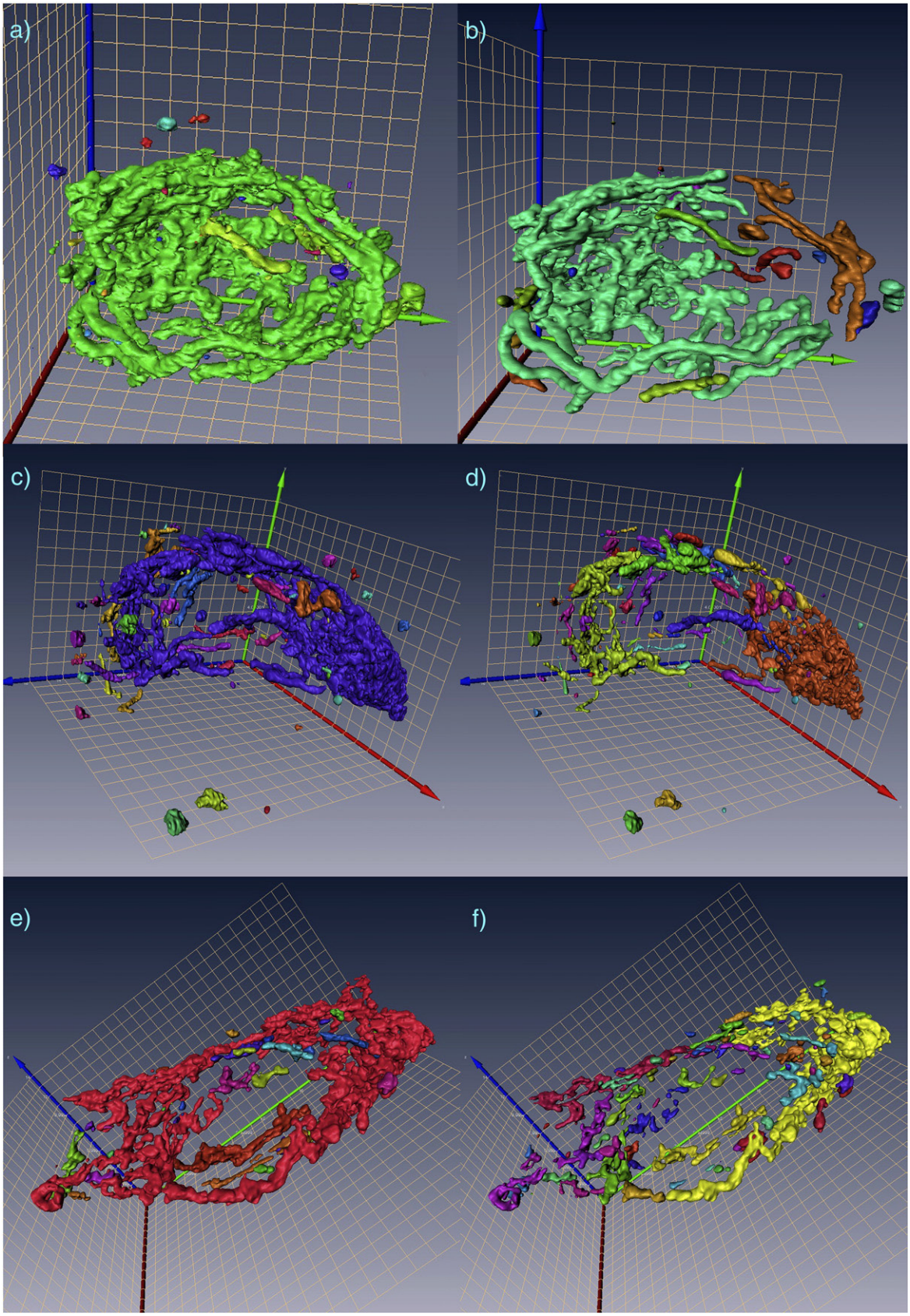

Fig. 4. *Iso*-surface projections for 4Pi imaging of mitochondrial network in β-cells of control (Wistar) and diabetic Goto Kakizaki rats. Unlike non-diabetic phenotype ($I_T = 20$: panel a); $I_T = 40$: panel b)), the diabetic phenotype in the Goto Kakizaki rats was manifested by higher disintegration apparent at $I_T = 40$ (panels d) and f) showing two different islet samples) in *iso*-surface projections. Certain disintegration is recognized also at $I_T = 20$ (panels c) and e)), which represents the minimum noise levels subtracted. *Iso*-surface mode 3D projections were created with Amira 5.2.2. A 1 μm 3D grid is shown in the background. Color-coding is used to distinct the different objects. Color-coding for axes: green — *Z* axis; red — *X* axis; blue — *Y* axis.

3. Results

3.1. Verification of nearly completely interconnected mitochondrial network in INS-1E cells

The superior 3D resolution of 4Pi microscopy over that of conventional confocal microscopy is an excellent tool to resolve the interconnectivity of mitochondrial networks compared to methods that rely on conventional confocal microscopy, especially when only 2D images are taken [23]. It is however crucial to avoid interconnectivity artifacts by a careful determination of threshold levels I_T as described in the Materials and methods section. Examples are shown for a section of an INS-1E cell as a suitable β-cell model (Fig. 1A) and another INS-1E cell with the mitochondrial network artificially disintegrated by 20 μM rotenone (Fig. 1B). The optimization procedure in fact analyzes noise. Data points of low intensities but of high incidence are clearly recognized in the histograms (Fig. 1C) and hence must be removed from the images. Fig. 1C clearly shows that a large amount of noise exists in the image at intensity levels 1 to 10. Consequently, when using $I_T = 5$, the data still contain noise (cf. Fig. 2a). For *iso*-surface plots, connecting borders of signal intensity just at I_T, it brings artificial blebs, artificially thick mitochondrial tubules

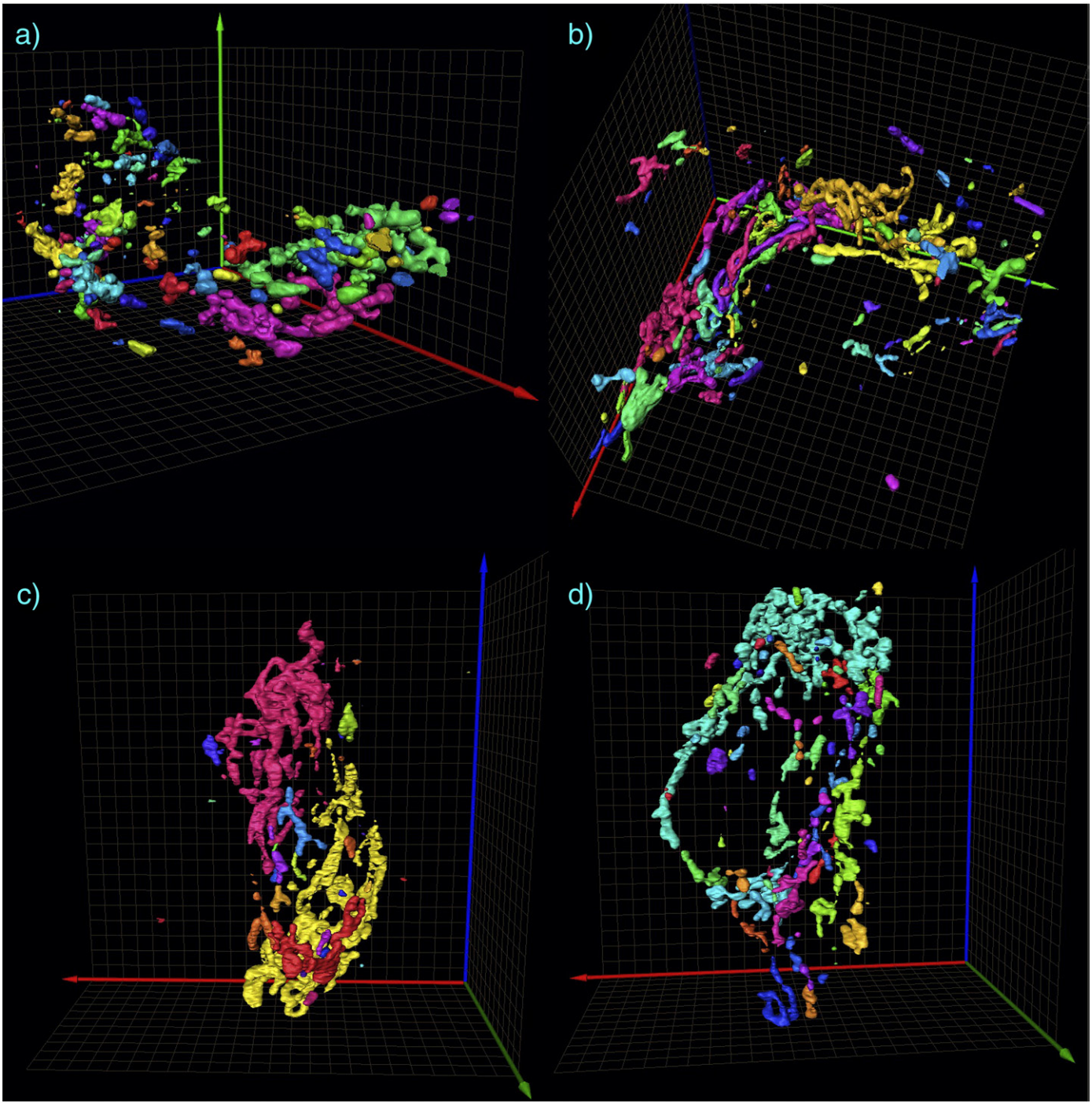

Fig. 5. 4Pi imaging of mitochondrial network in selected diabetic β-cells of Goto Kakizaki rats. Diabetic phenotype in the Goto Kakizaki rats is manifested by disintegration of originally highly interconnected mitochondrial reticulum as observed in control β-cells. *Iso*-surface mode 3D projections with $I_T = 40$ were created with Amira 5.2.2. A 1 μm 3D grid is shown in the background. Color-coding is used to distinct the different objects. Color-coding for axes: green — *Z* axis; red — *X* axis; blue — *Y* axis.

(Fig. 1Aa), and unrealistic connections (Fig. 1Bb). In turn, at higher I_T values, the *iso*-surface plots can display artificial fragmentation (Fig. 1Ad; Bh). Hence, in order to compare two samples, a series of *iso*-surface plots with increasing I_T values are required together with the noise analysis given by histograms.

Alternative visual noise analysis can be carried out by inspecting plots showing representations of the original 3D data such as "Radiosity" plots of Paraview software (Fig. 1Ba, Bc) or Voltex plots of Amira 5.2.2 software (Fig. 2). Besides the *iso*-surface plots (Figs. 3–5) the latter software offers "Autoskeleton module", yielding representations such as in Fig. 6. For the best analysis, all three methods are required to analyze 3D data from 4Pi microscope and to judge with certainty, whether network is disintegrated or interconnected, and to estimate its features.

3.2. Interpretation of the signal distribution in 4Pi images

4Pi microscopy allows to determine the tubule thickness independently from the intensity of the tubule by analyzing the axial profile [9]. This is important since the apparent signal level of a tubule section itself cannot be used as a reliable indicator for the tubule's thickness but merely the amount of mRoGFP present in this section. Assuming that the mRoGFP-concentration is relatively constant throughout the mitochondrial matrix, the brightness reflects a combination of tubule thickness (*i.e.* the diameter of the outer mitochondrial membrane) and cristae morphology which can severely reduce the matrix volume. Especially the lateral (xy) resolution of 4Pi microscopy is not sufficient to resolve substructures in mitochondria. The resulting lateral smoothing effect obscures any substructure in the tubules and automatically leads to a signal maximum close to the central axis of the tubules (Fig. 1B). This observation does therefore not necessarily require that the mRoGFP is highest at that location (even if it is so most likely).

We do not observe a strong variation of the mRoGFP signal along the tubule axes. This suggests, that neither the tubule diameter nor the overall cristae structure changes drastically over short length scales. Additionally, tubules within the same cell are of comparable intensity confirming a fairly narrow thickness distribution within the network as observed before [23].

3.3. Islet β-cells contain similar dense mitochondrial network as INS-1E cells

Overcoming pitfalls in the analysis of 3D 4Pi data, we encountered another obstacle when the bi-objective imaging inherent to 4Pi microscopy had to be applied to a big cell cluster such a Langerhans islet. We used the low efficiency of transfection to our advantage, since having only a few cells with mRoGFP-transfected mitochondria enabled us to distinguish single β-cells within the islet. The β-cell identification was assisted by the fluorescent immunostaining against β-cell specific GLUT2 as a surface antigen. This identification was essential for islets from Goto Kakizaki rats where insulin-positive β-cells are present in a minor fraction, as compared to 85% in healthy (control) islets [37,38]. However, even when selecting a β-cell near the surface of the islet (and thus closer to one of the objectives), the second objective has to excite and collect emitted fluorescence through the many cells of the whole islet. This general obstacle for 4Pi microscopy has been solved by simply selecting small islets ($z<70$ μm) for imaging after their transfection and fixation.

We first tested samples using both 3D and 2D imaging by conventional confocal microscope (Fig. 3). Specifically, 3D *iso*-surface plots constructed from the obtained data for control β-cells of Wistar rats (Fig. 3a,b,c,d) and diabetic β-cells of Goto Kakizaki rats (Fig. 3e,f) did not show any significant distinction. When viewed by an angle that included the worse *z*-axis resolution of conventional confocal microscopy, the presumed tubular structure was blurred into apparently fused columns (Fig. 3b,d,f). Also 2D conventional images, selecting random mitochondrial network sections of β-cells of non-diabetic (Fig. 3g) or diabetic Langerhans islets (Fig. 3h), were of a nearly indistinguishable pattern.

The optimized procedure for 3D 4Pi imaging of mitochondrial network in lentivirally transfected Langerhans islets with mRoGFP-constructs yielded superior 3D reconstructions of mitochondrial networks within the β-cells of isolated Langerhans islets as displayed by the three ways described (Figs. 2 and 4–6). The 4Pi images allow to distinguish significantly different features of the mitochondrial networks in control and diabetic β-cells. One can clearly see that β-cells of control Langerhans islets show equally dense and highly interconnected mitochondrial networks (Figs. 2a,b, 4a,b, and 6a,b) as INS-1E cells (Fig. 1A). When increasing the *iso*-surface threshold in 3D displays, the network still contains a single highly connected reticulum plus one or less frequently several small reticula separated, such as observed at an I_T value of 40 (Fig. 4b).

3.4. Mitochondrial network in β-cells of diabetic Goto Kakizaki rats is more disintegrated

β-cells, which were still displaying the GLUT2 antigen, in Langerhans islets isolated from diabetic Goto Kakizaki rats exhibited in five evaluated islets a more disintegrated network, when compared with non-diabetic islets. Examples with the most disintegrated networks are shown in Figs. 2c,d, 4c,d,e,f and 5. This conclusion can be rigorously derived from the fact that when increasing the *iso*-surface threshold in 3D displays (Fig. 4c,d and e,f, for the second sample), the network is more disintegrated at I_T of 40 (Fig. 4d,f). Note that a higher disintegration state of the mitochondrial network does not necessarily reflect ongoing apoptosis. Indeed, islets of Goto Kakizaki rats in parallel samples were respiring, although having impaired glucose-stimulated insulin secretion as measured either directly or as coupled state of respiring islet mitochondria (not shown).

3.5. Analysis of volume distribution pattern and signal density distribution pattern

From the histograms of intensity distribution over 256 signal levels, we estimated that the main noise level is below 10. Histograms (e.g. Fig. 1C) for all samples had the same shape and we concluded that it is legitimate to compare samples at the same I_T levels. The three-point deconvolved 4Pi data, *i.e.* data still including the background noise, typically gave signal from two thirds of the 3D imaged volume. After a proper background subtraction only ~5% of the 3D imaged volume was occupied by the mitochondrial network. The mRoGFP-accessible space, *i.e.* mitochondrial matrix, can be ascribed to the "complete" volume with subtracted noise, *i.e.* at I_T levels of 10 and higher; alternatively signals of higher intensities but comprising lower volumes of typically 67% and 40–45% are calculated at I_T levels of 20 and 40, respectively, when compared to 100% calculated on the basis of I_T of 10.

Having adjusted signal and optimum I_T levels, we analyzed number and volume size of the objects in the images of mitochondrial reticulum of non-diabetic and diabetic β-cells. Fig. 7 shows the

Fig. 6. "Autoskeleton" projections of 4Pi imaging of mitochondrial network in β-cells of control (Wistar) and diabetic Goto Kakizaki rats. Unlike for control β-cells (a,b), diabetic phenotype of islet β-cells from the Goto Kakizaki rats (four different diabetic β-cells are represented in panels c,d,e,f) is manifested also in "Autoskeleton" projections created with Amira 5.2.2. A 1 μm 3D grid is shown in the background. Color-coding for axes: green — *Z* axis; red — *X* axis; blue — *Y* axis.

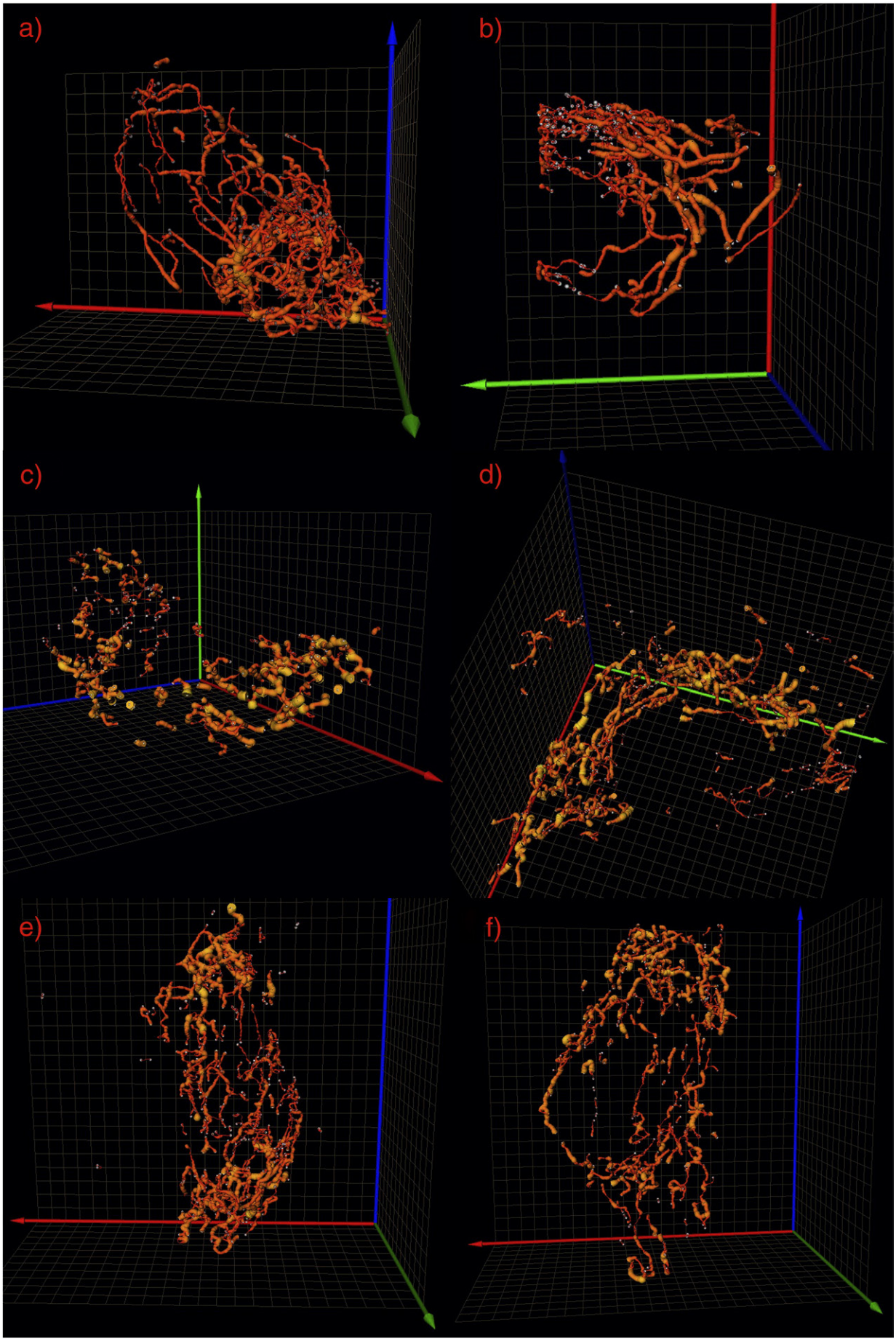
a)
b)
c)
d)
e)
f)

distribution of a relative volume for fragments of mitochondrial reticulum at I_T levels of 20 for control and diabetic β-cell networks. The relative volumes of fragments (as percentage of the largest one) describe distinction between control and diabetic β-cell networks very clearly. Non-diabetic mitochondria exhibit volume of the second, third, fourth, *etc.*, fragments relative volume, significantly lower than diabetic ones. This indicates that in non-diabetic cells the mitochondrial network consists of mainly one large mitochondrion with only a few small isolated fragments. In diabetic cells, in contrast, several fragments of intermediate size exist, showing more frequent fragmentation. In extreme cases, the diabetic β-cells exhibited a completely disintegrated mitochondrial reticulum with numerous small spherical and short segment objects (Figs. 2d, 5a, and 6c).

3.6. Other parameters of islet β-cell mitochondrial network

The average tubule diameter of non-diabetic islet β-cell mitochondria taken by the "interferometric" method (derived from point spread functions) and "ruler" method (measuring distances on original xz stacks) was 230 ± 47 nm ($n = 50$) and 214 ± 16 nm ($n = 60$), respectively, *i.e.* significantly smaller than the values of 270 ± 28 nm and 270 ± 40 nm, respectively, previously reported for INS-1E cells [23]. The tubule (object) diameter in diabetic β-cells was slightly higher, on average 279 ± 48 nm ($n = 72$) and 236 ± 27 nm ($n = 100$) as taken by the "interferometric" and "ruler" method, respectively. The diameter distributions revealed that in diabetic β-cells a higher portion of diameters of 250 nm and above exists, whereas in controls the most frequent diameters are below 250 nm (Fig. 8a,b).

Other major parameters (Table 1), such as the number of branching points and number of "double diameter" segments or bigger "cisternae" located at bifurcations and branching points, exhibited the same pattern as revealed for mitochondrial network of INS-1E cells [23]. In contrast, non-diabetic islet β-cells contain a higher number of regions where tubules are fused into more bulky cisternae, as well as tubules of about twice the "norma" diameter, and irregular shapes (Figs. 2a,b and 4–6), when compared to INS-1E cells (Fig. 1A) [23]. Disintegration of the network in diabetic β-cells reduced also the number of these cisternae (Table 1.).

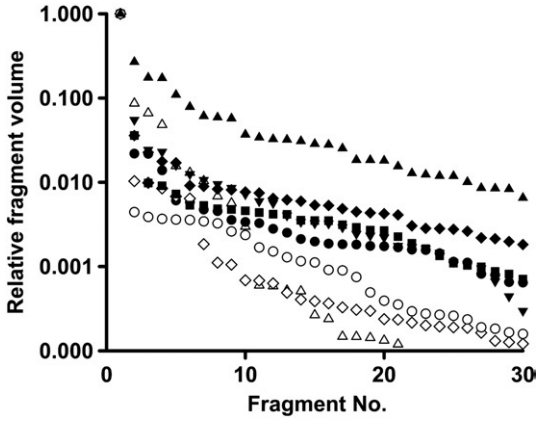

Fig. 7. Distribution of relative fragment volume (related to the maximum one) for mitochondrial network of β-cells of Langerhans islets from non-diabetic Wistar and diabetic Goto Kakizaki rats. The fragmentation analysis of 3D data is shown for three non-diabetic β-cells (open symbols) and five diabetic β-cells (close symbols) for isolated Langerhans islets from Wistar rats and Goto Kakizaki rats, respectively. The volume of the largest mitoreticulum (fragment) present in each cell was set to 1 and the other fragments were related to it as fractions of this unit volume. The relative volume is then plotted against the number of objects of each volume size.

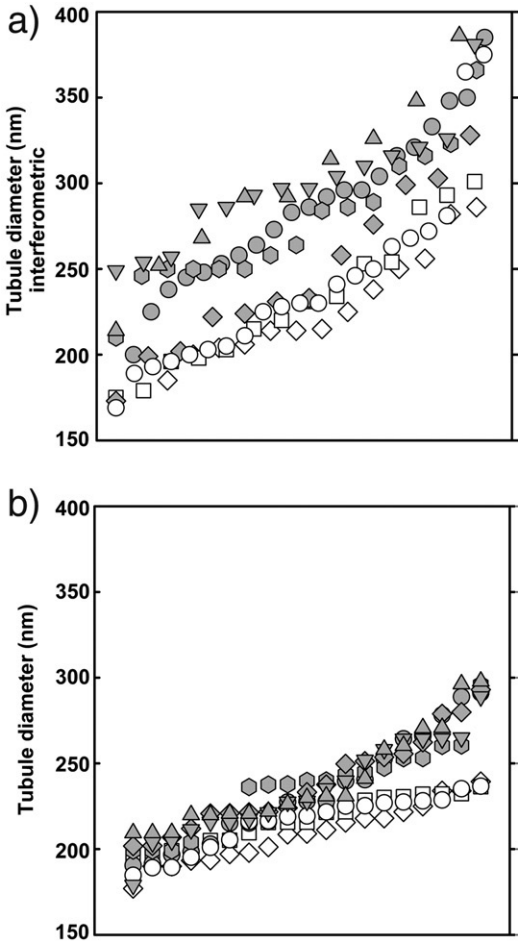

Fig. 8. Charts of tubule diameter variance for mitochondrial network of β-cells of Langerhans islets from non-diabetic Wistar and diabetic Goto Kakizaki rats. a) Interferometric method; b) ruler method. The data of three control and five diabetic β-cells were evaluated by the given method for variance of tubules diameters in islet β-cells of non-diabetic Wistar rats (open symbols) and diabetic Goto Kakizaki rats (grey symbols).

4. Discussion

Using 4Pi microscopy for the 3D imaging of mitochondrial matrix-addressed RoGFP, we could observe, to our knowledge for the first time, that also *in vivo* cells within the tissue such as pancreatic islet β-cells form strongly interconnected mitochondrial reticulum consisting of mainly a single large mitochondrion or a few (up to five, but largely interconnected reticula). Consequently, it is plausible that the networks frequently observed in cultured cells cannot be an artifact of cell cultivation (see e.g. [23]). An advantage of a continuous mitochondrial network may be seen in the coordinated membrane potential changes throughout the whole reticulum and in an accessibility of the entire network for the transcription and expression products of mitochondrial DNA. Recently, it has also been suggested that mitochondrial networking protects β-cells from nutrient-induced apoptosis [43]. In turn, using the diabetic Goto Kakizaki rats and their remaining β-cells in Langerhans islets as a T2DM model, we could demonstrate that this single mitochondrion tends to become more disintegrated under pathological conditions. These islets usually contain far less insulin-positive β-cells and instead are protruded by fibroblasts and other cell types [37,38]. Although we have observed here only a single pathogenesis, the generalized principle of morphological diagnostics involving the mitochondrial network may be based upon altered mitochondrial dynamics and morphology under a variety of pathological conditions. This raises the

Table 1
Diameters of tubules and other characteristics of mitochondrial networks in primary β-cells of control and diabetic Langerhans islets. Diameters evaluated by the two ways as described in Materials and methods are listed for selected images of Langerhans islet β-cells. There were 13 to 20 estimates and 20 estimates for interferometric and ruler method, respectively. Data of all samples control or diabetic were also averaged ("Average"). "Cisternae" are defined as "double diameter" segments or bigger objects located at bifurcations and branching points.

Rat model	Diameter (interferometric method) (nm)	Diameter (ruler method) (nm)	No. of reticula at I_T 20 (I_T 40)	No. of spheres at I_T 20 (I_T 40)	No. of short segments at I_T 20 (I_T 40)	No. of cisternae
Control (Wistar) average	230 ± 47 nm	214 ± 16 nm				
Sample 1	215 ± 46 nm	209 ± 14 nm	1 (1)	9 (10)	6 (5)	40
Sample 2	231 ± 40 nm	217 ± 12 nm	1 (3)	8 (10)	12 (15)	25
Sample 3	240 ± 50 nm	215 ± 13 nm	1 (1)	4 (10)	4 (10)	10
Diabetic — average (Goto Kakizaki)	279 ± 48 nm	236 ± 27 nm				
Sample 1	279 ± 55 nm	233 ± 27 nm	1 (4)	15 (15)	5 (10)	20
Sample 2	298 ± 33 nm	234 ± 23 nm	2 (3)	15 (10)	15 (34)	5
Sample 3	277 ± 38 nm	236 ± 18 nm	1 (0)	25 (25)	37 (71)	3
Sample 4	299 ± 48 nm	239 ± 23 nm	1 (2)	15 (10)	15 (34)	3

question, why for β-cells of Goto Kakizaki rats their pro-fission mitochondrial dynamics prevails. A possible explanation is that this is the result of previously reported lower mtDNA contents (indicated by the lower 12S rRNA and cyt *b* mRNA) in islets of adult Goto Kakizaki rats [39]. One might speculate that the increased mitophagy could explain such a lower mtDNA content. Since, it has been suggested that mitochondrial degradation, including mtDNA degradation, proceeds specifically in small objects disintegrated from the main mitochondrial reticulum [47], our current finding of numerous disintegrated small objects in diabetic Goto Kakizaki rats well confirms this view. Also, a significantly smaller mitochondrial volume and an increased number of mitochondria per unit tissue volume have been reported in β-cells of Goto Kakizaki rats [39], which perfectly match our observations.

Goto Kakizaki rats were also reported to possess an impaired glucose-stimulated insulin secretion that originates also from insufficient coupling of mitochondria and insufficient levels of ATP synthesis upon glucose entry into β-cells [37,38]. We noted previously an emerging importance of autocrine role of insulin in pancreatic β-cells [46] and this might be an accelerating pathogenic factor playing a role also in the altered (disintegrated) mitochondrial network morphology [23]. Indeed, 4Pi microscopic images for INS-1E cells cultivated at 5 mM glucose [23], *i.e.* with insufficient autocrine insulin, contain similar features as diabetic β-cells of Goto Kakizaki rats. These features are represented namely by a more fragmented state (Table 1).

We want to point out that conventional confocal microscopy has been unable to distinguish between patterns of non-diabetic and diabetic mitochondrial networks when used in 2D or 3D mode (Fig. 3). Similarly, even though electron microscopy (EM) routinely achieves a resolution <10 nm, EM has difficulties revealing the extended and connected mitochondrial networks. Classic EM staining procedures disrupt the mitochondrial network. Even with the recent advent of cryo-EM methods for sample preservation, it is a time consuming procedure to assemble a 3D image from a series of electron microscopic or tomographic images which is still prone to artifacts or severely limited in sample thickness. Nevertheless, successful reconstruction of mitochondrial network in Langerhans islet β-cells show rather disintegrated pattern of such network [48]. The discrepancy between this results and our 4Pi data and conventional confocal microscopic images in numerous reports is not well understood. However, the noise analyses for 3D data apply to the same principles as outlined in this work and without a proper noise analysis any 3D reconstructions should be taken with a caution. In spite of this, both EM tomography [48] and conventional EM of β-cells either from INS1E cells or isolated islets indicated similar mitochondrial tubule diameter (minimum of tubular sections) [46] as determined by 4Pi microscopy ([6] and this work). Conventional EM, providing sections of mitochondrial tubules, the well-known solitary kidney-shaped mitochondria images, has already been employed for ultramorphological diagnostics related to T2DMM. It has been reported that pancreatic β-cells of human islets isolated from diabetic donors exhibit mitochondria with a higher volume than mitochondria from islets of healthy donors [49]. Additionally, mitochondria of diabetic heart possess thicker mitochondrial reticulum than in control hearts [50,51].

Although the resolution improvement of 4Pi microscopy over conventional confocal microscopy affects only the *z*-axis, 3D images of mitochondrial network taken by conventional confocal microscopy are blurred into apparently fused columns (Fig. 3). The network can be fully resolved by the enhanced 3D imaging capabilities provided by techniques such as 4Pi microscopy. As a consequence, we were able to measure subtle but, as we believe, significant changes of β-cell mitoreticulum morphology between control (Wistar) and diabetic Goto Kakizaki rats by careful 3D image analysis. The apparent stronger disintegration at higher *iso*-surface thresholds might be a result of not only more gaps between tubules of the mitochondrial network, but by a principally different density distribution of the mRoGFP-accessible matrix volume. In other words, the additional difference in patterns could be a result of the differences in internal cristae morphology (cf. [49]).

New emerging super-resolution fluorescence microscopy techniques next to 4Pi microscopy also start to provide means to characterize mitochondrial cristae morphology. Stimulated emission depletion (STED) microscopy [10–12,52], first realized in 1994 [11], is overcoming Abbe's resolution limit by combining laser scanning microscopy with actively switching off fluorescent probes in the outskirts of the laser focus. This limits fluorescence emission to the center of the excitation laser focus and results in an effective lateral focus size (and hence resolution) of typically 25–70 nm (and better) across [10–12,52]. In most STED configurations, the axial (*z*-axis) resolution remains at the conventional confocal value, *i.e.* ~700 nm. To get a true 3D sub-diffraction resolution, STED has been combined with the 4Pi principle in a technique called *iso*-STED in which a true 3D resolution of ~45 nm has been achieved using organic Atto dyes [13,14]. The *iso*-STED technique has been successfully used to reconstruct a part of the mitochondrial tubule outer membrane (immunostained) three-dimensionally confirming the typical diameter of mitochondrial tubules of around ~250 nm [13]. Recently, *iso*-STED has also been able to resolve cristae sacks in combination with the outer membrane contour of mitochondrial tubules [14]. Unfortunately, the commercialization of *iso*-STED and the availability of a ready-to-use instrument for biomedical research still await development.

In 2006, a new fluorescence wide-field microscopy-based technique has been developed which also achieves resolution well below 100 nm. Termed fluorescence photoactivation localization microscopy (FPALM [17]), PALM [16] or stochastic optical reconstruction microscopy (STORM [15]) and published by three groups practically simultaneously, this technique takes an advantage of

photophysically switching fluorescent probes [53,54]. Instead of imaging all fluorescent probes at the same time, only a small fraction of photoactivatable (or photoswitchable) fluorophores is activated at any time and its fluorescence detected. The fraction of molecules is activated stochastically and at such a low density that the activated probes can be imaged as single molecules. Utilizing algorithms well known from particle-tracking experiments over decades, these molecules can be localized to a much better accuracy than the width of their diffraction-limited images. Bleaching and subsequent imaging of many of these fractions (typically thousands), and combination of the determined particle positions finally renders a 2D image with 20 to 40 nm resolution. This scheme which had been originally proposed for 2D imaging recently got expanded to 3D imaging [18–21] and is now able to image sub-cellular structures at sub-100 nm 3D resolution. Mitochondria have been successfully used as test objects to demonstrate the imaging capabilities of these techniques (Bewersdorf et al., unpublished), which promises a bright future for imaging-based mitochondria research with these techniques. New 3D super-resolution measurements by *iso*-STED [13,14] also confirm our assumption that the diameter of mitochondria is independent from the orientation of the measurement.

Of key interest in sub-mitochondrial imaging will be mitochondrial DNA (mtDNA) which plays a major role for a majority of mitochondrial pathologies, or is affected during their development, since it encodes 13 key subunits of respiratory chain and ATP synthase. mtDNA is severely affected by oxidative stress, transformed into its mutations, which further elevates the stress and a vicious circle is set, resulting in diseases and aging [24,25]. Organization of mtDNA is as complex as it is for nuclear chromatin, however, the micro-universe of mtDNA is yet completely unexplored [24,55]. For example, it is not known, whether mtDNA transcription proceeds independently from replication, when the replication is initiated during the cell cycle, and what is the role of triplicate DNA structures (even bifurcations in mtDNA, a “mtDNA network” has been reported [56]).

For the study of mitochondria network morphology, however, 4Pi microscopy and techniques which offer a comparable resolution such as I^5M [57] and structured illumination microscopy [58,59] provide sufficient resolution as demonstrated here. These techniques have the advantage that they can readily utilize well established fluorescent markers such as GFP and mRoGFP. Additionally, some of them are commercially available which allows access to this technology to a larger group of users.

Acknowledgements

Cell cultivation by Lenka Josková and help of Martin Bartoš (Alef, Ltd., Prague) with 3D image displays and analysis are gratefully acknowledged. We thank the staff of The Jackson Laboratory's Scientific Services for their overall support. The project was supported by the grant NR/9183-3 from the Czech Ministry of Health; IAA500110701 and AV0Z50110509 from the Academy of Sciences. Travelling to partner laboratory has been supported by the Czech Ministry of Education (ME09029). Funding for the 4Pi microscope at The Jackson Laboratory was provided by the W. M. Keck Foundation and National Science Foundation Grant DBI-0421007.

References

[1] S.W. Hell, E.H.K. Stelzer, Properties of a 4Pi-confocal fluorescence microscope, J. Opt. Soc. Am. A. 9 (1992) 2159–2166.
[2] S.W. Hell, E.H.K. Stelzer, Fundamental improvement of resolution with a 4Pi-confocal fluorescence microscope using two-photon excitation, Opt. Commun. 93 (1992) 277–282.
[3] K. Bahlmann, S. Jakobs, S.W. Hell, 4Pi-confocal microscopy of live cells, Ultramicroscopy 87 (2001) 155–164.
[4] H. Gugel, J. Bewersdorf, S. Jakobs, J. Engelhardt, R. Storz, S.W. Hell, Cooperative 4Pi excitation and detection yields sevenfold sharper optical sections in live-cell microscopy, Biophys. J. 87 (2004) 4146–4152.
[5] J. Bewersdorf, B.T. Bennet, K.L. Knight, H2AX chromatin structures and their response to DNA damage revealed by 4Pi microscopy, Proc. Natl. Acad. Sci. U. S. A. 103 (2006) 18137–18142.
[6] R. Medda, S. Jakobs, S.W. Hell, J. Bewersdorf, 4Pi microscopy of quantum dot-labeled cellular structures, J. Struct. Biol. 156 (2006) 517–523.
[7] S. Jakobs, High resolution imaging of live mitochondria, Biochim. Biophys. Acta 1763 (2006) 561–575.
[8] M.C. Lang, J. Engelhardt, S.W. Hell, 4Pi microscopy with linear fluorescence excitation, Opt. Lett. 32 (2007) 259–261.
[9] A. Egner, S. Jakobs, S.W. Hell, Fast 100-nm resolution three-dimensional microscope reveals structural plasticity of mitochondria in live yeast, Proc. Natl. Acad. Sci. U. S. A. 99 (2002) 3370–3375.
[10] S.W. Hell, Far-field optical nanoscopy, Science 316 (2007) 1153–1158.
[11] S.W. Hell, J. Wichmann, Breaking the diffraction resolution limit by stimulated emission: stimulated-emission-depletion fluorescence microscopy, Opt. Lett. 19 (1994) 780–782.
[12] B. Hein, K.I. Willig, S.W. Hell, Stimulated emission depletion (STED) nanoscopy of a fluorescent protein-labeled organelle inside a living cell, Proc. Natl. Acad. Sci. U. S. A. 105 (2008) 14271–14276.
[13] R. Schmidt, C.A. Wurm, S. Jakobs, J. Engelhardt, A. Egner, S.W. Hell, Spherical nanosized focal spot unravels the interior of cells, Nat. Methods 5 (2008) 539–544.
[14] R. Schmidt, C.A. Wurm, A. Punge, A. Egner, S. Jakobs, S.W. Hell, Mitochondrial cristae revealed with focused light, Nano Lett. 9 (2009) 2508–2510.
[15] M.J. Rust, M. Bates, X. Zhuang, Sub-diffraction-limit imaging by stochastic optical reconstruction microscopy (STORM), Nat. Methods 3 (2006) 793–795.
[16] E. Betzig, G.H. Patterson, R. Sougrat, O.W. Lindwasser, S. Olenych, J.S. Bonifacino, M.W. Davidson, J. Lippincott-Schwartz, H.F. Hess, Imaging intracellular fluorescent proteins at nanometer resolution, Science 313 (2006) 1642–1645.
[17] S.T. Hess, T.P.K. Girirajan, M.D. Mason, Ultra-high resolution imaging by fluorescence photoactivation localization microscopy, Biophys. J. 91 (2006) 4258–4272.
[18] B. Huang, W. Wang, M. Bates, X. Zhuang, Three-dimensional super-resolution imaging by stochastic optical reconstruction microscopy, Science 319 (2008) 810–813.
[19] M.F. Juette, T.J. Gould, M.D. Lessard, M.J. Mlodzianoski, B.S. Nagpure, B.T. Bennett, S.T. Hess, J. Bewersdorf, 3D sub-100 nm resolution by biplane fluorescence photoactivation localization microscopy, Nat. Methods 5 (2008) 527–529.
[20] S.R. Pavani, M.A. Thompson, J.S. Biteen, S.J. Lord, N. Liu, R.J. Twieg, R. Piestun, W.E. Moerner, Three-dimensional, single-molecule fluorescence imaging beyond the diffraction limit by using a double-helix point spread function, Proc. Natl. Acad. Sci. U S A 106 (2009) 2995–2999.
[21] G. Shtengel, J.A. Galbraith, C.G. Galbraith, J. Lippincott-Schwartz, J.M. Gillette, S. Manley, R. Sougrat, C.M. Waterman, P. Kanchanawong, M.W. Davidson, R.D. Fetter, H.F. Hess, Interferometric fluorescent super-resolution microscopy resolves 3D cellular ultrastructure, Proc. Natl. Acad. Sci. U S A 106 (2009) 3125–3130.
[22] J. Bereiter-Hahn, M. Voth, Dynamics of mitochondria in living cells: shape changes, dislocations, vision and fission of mitochondria, Microsc. Res. Tech. 27 (1994) 198–219.
[23] L. Plecitá-Hlavatá, M. Lessard, J. Šantorová, J. Bewersdorf, P. Ježek, Mitochondrial oxidative phosphorylation and energetic status are reflected by morphology of mitochondrial network in INS-1E and HEP-G2 cells viewed by 4Pi microscopy, Biochim. Biophys. Acta 1777 (2008) 834–846.
[24] P. Ježek, L. Plecitá-Hlavatá, Mitochondrial reticulum network dynamics in relation to oxidative stress, redox regulation, and hypoxia, Int. J. Biochem. Cell Biol. 41 (2009) 1790–1804.
[25] P.H.G.M. Willems, J.A.M. Smeitink, W.J.H. Koopman, Mitochondrial dynamics in human NADH:oxidoreductase deficiency, Int. J. Biochem. Cell Biol. 41 (2009) 1773–1783.
[26] S. Ravera, I. Panfoli, D. Calzia, M.G. Aluigi, P. Bianchini, A. Diaspro, G. Mancardi, A. Morelli, Evidence for aerobic ATP synthesis in isolated myelin vesicles, Int. J. Biochem. Cell Biol. 41 (2009) 1581–1591.
[27] I. Panfoli, D. Calzia, P. Bianchini, S. Ravera, A. Diaspro, G. Candiano, A. Bachi, M. Monticone, M.G. Aluigi, S. Barabino, G. Calabria, M. Rolando, C. Tacchetti, A. Morelli, I.M. Pepe, Evidence for aerobic metabolism in retinal rod outer segment disks, Int. J. Biochem. Cell Biol. 41 (2009) 2555–2565.
[28] M. Friederich, P. Hansell, F. Palm, Diabetes, oxidative stress, nitric oxide and mitochondria function, Curr. Diabetes Rev. 5 (2009) 120–144.
[29] J. Szendroedi, M. Roden, Mitochondrial fitness and insulin sensitivity in humans, Diabetologia 51 (2008) 2155–2167.
[30] N. Li, F. Frigerio, P. Maechler, The sensitivity of pancreatic beta-cells to mitochondrial injuries triggered by lipotoxicity and oxidative stress, Biochem. Soc. Trans. 36 (2008) 930–934.
[31] G.A. Rutter, L.E. Parton, The beta-cell in type 2 diabetes and in obesity, Front. Horm. Res. 36 (2008) 118–134.
[32] K. Højlund, H. Beck-Nielsen, Impaired glycogen synthase activity and mitochondrial dysfunction in skeletal muscle: markers or mediators of insulin resistance in type 2 diabetes? Curr. Diabetes Rev. 2 (2006) 375–395.
[33] L.E. Fridlyand, L.H. Philipson, Reactive species, cellular repair and risk factors in the onset of type 2 diabetes mellitus: review and hypothesis, Curr. Diabetes Rev. 2 (2006) 241–259.
[34] A.P. Rolo, C.M. Palmeira, Diabetes and mitochondrial function: role of hyperglycemia and oxidative stress, Toxicol. Appl. Pharmacol. 15 (2006) 167–178.
[35] P. Maechler, C.B. Wollheim, Mitochondrial function in normal and diabetic beta-cells, Nature 414 (2001) 807–812.
[36] P. Finocchietto, F. Barreyro, S. Holod, J. Peralta, M.C. Franco, C. Méndez, D.P. Converso, A. Estévez, M.C. Carreras, J.J. Poderoso, Control of muscle mitochondria by insulin entails activation of Akt2-mtNOS pathway: implications for the metabolic syndrome, PLoS ONE 3 (2008) e1749.

[37] H. Mizukami, R. Wada, M. Koyama, T. Takeo, S. Suga, M. Wakui, S. Yagihashi, Augmented β cell loss and mitochondrial abnormalities in sucrose-fed GK rats, Virchows Arch. 452 (2008) 383–392.
[38] C.-G. Ostenson, S. Efendic, Islet gene expression and function in type 2 diabetes; studies in the Goto–Kakizaki rat and humans, Diabetes Obes. Metab. 9 (S2) (2007) 180–186.
[39] P. Serradas, M.H. Giroix, C. Saulnier, M.N. Gangnerau, L.A. Borg, M. Welsh, B. Portha, N. Welsh, Mitochondrial deoxyribonucleic acid content is specifically decreased in adult, but not fetal, pancreatic islets of the Goto–Kakizaki rat, a genetic model of noninsulin-dependent diabetes, Endocrinol. 136 (1995) 5623–5631.
[40] W. Shen, J. Hao, C. Tian, J. Ren, L. Yang, X. Li, C. Luo, C.W. Cotma, J.A. Liu, A combination of nutriments improves mitochondrial biogenesis and function in skeletal muscle of type 2 diabetic Goto–Kakizaki rats, PLoS One 3 (2008) e2328.
[41] G. Benard, N. Bellance, D. James, P. Parrone, H. Fernandez, T. Letellier, R. Rossignol, Mutual control of mitochondrial bioenergetics and structural network organization, J. Cell Sci. 120 (2007) 838–848.
[42] P. Ježek, L. Plecitá-Hlavatá, K. Smolková, R. Rossignol, Distinctions and similarities of cell bioenergetics and role of mitochondria in hypoxia, cancer, and embryonic development, Int. J. Biochem. Cell Biol. 41 (2009).
[43] A.J. Molina, J.D. Wikstrom, L. Stiles, G. Las, H. Mohamed, A. Elorza, G. Walzer, G. Twig, S. Katz, B.E. Corkey, O.S. Shirihai, Mitochondrial networking protects beta-cells from nutrient-induced apoptosis, Diabetes 58 (2009) 2303–2315.
[44] R. Rossignol, R. Gilkerson, R. Aggeler, K. Yamagata, S.J. Remington, R.A. Capaldi, Energy substrate modulates mitochondrial structure and oxidative capacity in cancer cells, Cancer Res. 64 (2004) 985–993.
[45] A. Merglen, S. Theander, B. Rubi, G. Chaffard, C.B. Wollheim, P. Maechler, Glucose sensitivity and metabolism-secretion coupling studied during two-year continuous culture in INS-1E insulinoma cells, Endocrinology 145 (2004) 667–678.
[46] T. Špaček, J. Šantorová, K. Zacharovová, Z. Berková, L. Hlavatá, F. Saudek, P. Ježek, Glucose stimulated-insulin secretion of insulinoma INS1-E cells is associated with elevation of both respiration and mitochondrial membrane potential, Int. J. Biochem. Cell Biol. 40 (2008) 1522–1535.
[47] G. Twig, A. Elorza, A.J. Molina, H. Mohamed, J.D. Wikstrom, G. Walzer, L. Stiles, S.E. Haigh, S. Katz, G. Las, J. Alroy, M. Wu, B.F. Py, J. Yuan, J.T. Deeney, B.E. Corkey, O.S. Shirihai, Fission and selective fusion govern mitochondrial segregation and elimination by autophagy, EMBO J. 27 (2008) 433–446.
[48] A.B. Noske, A.J. Costin, G.P. Morgan, B.J. Marsh, Expedited approaches to whole cell electron tomography and organelle mark-up in situ in high-pressure frozen pancreatic islets, J. Struct. Biol. 161 (2008) 298–313.
[49] M. Anello, R. Lupi, D. Spampinato, S. Piro, M. Masini, U. Boggi, S. Del Prato, A.M. Rabuazzo, F. Purrello, P. Marchetti, Functional and morphological alternations of mitochondria in pancreatic beta cells from type 2 diabetic patients, Diabetologia 48 (2005) 282–289.
[50] X. Shen, S. Zheng, V. Thongboonkerd, M. Xu, W.M. Pierce, J.B. Klein, P.N. Epstein, Cardiac mitochondrial damage and biogenesis in a chronic model of type 1 diabetes, Am. J. Physiol. 287 (2004) E896–E905.
[51] D.L. Santos, C.M. Palmeira, R. Seiça, J. Dias, J. Mesquita, A.J. Moreno, M.S. Santos, Diabetes and mitochondrial oxidative stress: a study using heart mitochondria from the diabetic Goto–Kakizaki rat, Mol. Cell. Biochem. 246 (2003) 163–170.
[52] K.I. Willig, B. Harke, R. Medda, S.W. Hell, STED microscopy with continuous wave beams, Nat. Methods 4 (2007) 915–918.
[53] H. Shroff, C.G. Galbraith, J.A. Galbraith, H. White, J. Gillette, S. Olenych, M.W. Davidson, E. Betzig, Dual-color superresolution imaging of genetically expressed probes within individual adhesion complexes, Proc. Natl. Acad. Sci. U. S. A. 104 (2007) 20308–20313.
[54] M. Fernández-Suárez, Y.T. Ting, Fluorescent probes for superresolution imaging in living cells, Nat. Rev. Mol. Cell. Biol. 9 (2008) 929–943.
[55] J.N. Spelbrink, Functional organization of mammalian mitochondrial DNA in nucleoids: history, recent developments, and future challenges, IUBMB Life 62 (2010) 19–32.
[56] J.L. Pohjoismäki, S. Goffart, H. Tyynismaa, S. Willcox, T. Ide, D. Kang, A. Suomalainen, P.J. Karhunen, J.D. Griffith, I.J. Holt, H.T. Jacobs, Human heart mitochondrial DNA is organized in complex catenated networks containing abundant four-way junctions and replication forks, J Biol. Chem. 284 (2009) 21446–21457.
[57] M.G. Gustafsson, D.A. Agard, J.W. Sedat, I5M: 3D widefield light microscopy with better than 100 nm axial resolution, J. Microsc. 195 (1999) 10–16.
[58] P. Kner, B.B. Chhun, E.R. Griffis, L. Winoto, M.G. Gustafsson, Super-resolution video microscopy of live cells by structured illumination, Nat. Methods 6 (2009) 339–342.
[59] L. Schermelleh, P.M. Carlton, S. Haase, L. Shao, L. Winoto, P. Kner, B. Burke, M.C. Cardoso, D.A. Agard, M.G. Gustafsson, H. Leonhardt, J.W. Sedat, Subdiffraction multicolor imaging of the nuclear periphery with 3D structured illumination microscopy, Science 320 (2008) 1332–1336.